

The two-loop self-energy: diagrams in the coordinate-momentum representation

V.A. Yerokhin^a

Center for Advanced Studies, St. Petersburg State Polytechnical University, Polytekhnicheskaya 29,
St. Petersburg 195251, Russia

Received 29 January 2010 / Received in final form 15 March 2010
Published online 13 April 2010 – © EDP Sciences, Società Italiana di Fisica, Springer-Verlag 2010

Abstract. The paper reports a technique of evaluation of Feynman diagrams in the mixed coordinate-momentum representation. The technique is employed for a recalculation of the two-loop self-energy correction for the ground state of hydrogen-like ions with the nuclear charge numbers $Z = 10\text{--}30$. The numerical accuracy is considerably improved as compared to the previous calculations. The higher-order (in $Z\alpha$) remainder function is inferred from the numerical results and extrapolated towards $Z = 0$ and 1. The extrapolated value for hydrogen is consistent (but still not in perfect agreement) with the analytical result obtained within the perturbative approach.

1 Introduction

Investigations of the Lamb shift in atomic systems provide one of the most stringent tests of quantum electrodynamics (QED). They are also used for the determination of fundamental physical constants [1]. The main factors limiting the present theoretical understanding of the Lamb shift are the binding two-loop QED effects and, in particular, the two-loop self-energy correction.

Theoretical investigations of QED effects in light atoms traditionally rely on the perturbative expansion in the binding-strength parameter $Z\alpha$ (Z is the nuclear charge and α is the fine structure constant). The state of the art of such calculations is the evaluation of the dominant part of the two-loop correction to order $m\alpha^2(Z\alpha)^6$ [2–5]. The main problem of the $Z\alpha$ -expansion approach is the difficulty of estimation of uncalculated higher-order effects. In the case of the two-loop self-energy correction, the higher-order binding effects are larger than the experimental error both for the light systems (particularly, for the hydrogen atom [6]) and for the heavy ions [7–10].

The present investigation is based on the all-order approach which is nonperturbative in the parameter $Z\alpha$. The nonperturbative calculations started with the pioneering works of Wichmann and Kroll [11], Mohr [12,13], and Desiderio and Johnson [14]. For heavy ions, the all-order approach is the only alternative as the parameter of $Z\alpha$ is of order of unity. For light systems, this method is complementary to the $Z\alpha$ -expansion approach and can provide results for the higher-order remainder beyond the known $Z\alpha$ -expansion terms.

The all-order calculation of the two-loop self-energy correction depicted in Figure 1 was a long and difficult project accomplished in a series of papers [15–20]. The numerical results obtained in these studies agreed well with the first terms of the $Z\alpha$ expansion calculated within the perturbative approach. However, a significant disagreement was reported [19] for the contribution to order $m\alpha^2(Z\alpha)^6$ (the so-called B_{60} coefficient). Its reliable determination requires a high numerical accuracy to be achieved in all-order calculations for low values of Z , which is a challenging task. In our recent investigation [21], we briefly reported a new calculational technique for the evaluation of Feynman diagrams in the mixed coordinate-momentum representation. This technique significantly improved the numerical accuracy of the two-loop self-energy calculation and to a large extent removed the disagreement with the analytical approach. In the present paper, we present a detailed description of this calculational technique.

The relativistic units ($m = \hbar = c = 1$) and the Heaviside charge units ($\alpha = e^2/4\pi$, $e < 0$) will be used throughout the paper.

2 Two-loop self-energy

The Feynman diagrams representing the two-loop self-energy correction are shown in Figure 1. The contribution of the first diagram (Fig. 1a) is conveniently divided into two parts, the irreducible and the reducible one. The reducible part is induced by the virtual states with the energy $\varepsilon_n = \varepsilon_a$ in the middle electron propagator (ε_a is the energy of the reference state), and the irreducible part is the remainder. The irreducible part (often referred to as the loop-after-loop correction) can be interpreted as a

^a e-mail: yerokhin@pcqnt1.phys.spbu.ru

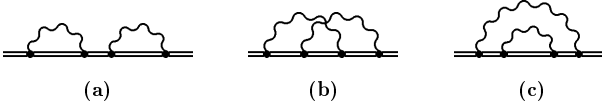


Fig. 1. Feynman diagrams representing the two-loop self-energy correction in the external binding field. The double line represents the electron propagating in the field of the nucleus.

second-order perturbation induced by the one-loop self-energy operator. The corresponding expression reads

$$\Delta E_{\text{LAL}} = \left\langle \gamma^0 \tilde{\Sigma}(\varepsilon_a) G^{\text{red}} \gamma^0 \tilde{\Sigma}(\varepsilon_a) \right\rangle, \quad (1)$$

where $\tilde{\Sigma}(\varepsilon_a) = \Sigma(\varepsilon_a) - \delta m$, $\Sigma(\varepsilon)$ is the one-loop self-energy operator [18], δm is the corresponding mass counterterm, and G^{red} is the reduced Dirac-Coulomb Green function. The irreducible part is finite and can be calculated separately by generalizing various methods developed for the one-loop self-energy. The reducible part is given by

$$\Delta E_{\text{red}} = \Delta E_{\text{SE}} \left\langle \gamma^0 \frac{\partial}{\partial \varepsilon} \tilde{\Sigma}(\varepsilon) \right\rangle_{\varepsilon=\varepsilon_a}, \quad (2)$$

where $\Delta E_{\text{SE}} = \langle \gamma^0 \tilde{\Sigma}(\varepsilon_a) \rangle$ is the one-loop self-energy correction.

The contribution induced by the diagram in Figure 1b will be referred to as the *overlapping* term. It is given by

$$\begin{aligned} \Delta E_O &= 2i\alpha \int_{-\infty}^{\infty} d\omega_1 \int d\mathbf{x}_1 \dots d\mathbf{x}_4 D(\omega_1, x_{13}) \psi_a^\dagger(\mathbf{x}_1) \\ &\times \alpha_\mu G(\varepsilon_a - \omega_1) \gamma^0 \Lambda^\mu(\varepsilon_a - \omega_1, \varepsilon_a) \psi_a(\mathbf{x}_4) - \delta m_O, \end{aligned} \quad (3)$$

where δm_O is the mass counterterm, $D(\omega, x_{12})$ is the radial part of the photon propagator in the Feynman gauge,

$$D(\omega, x_{12}) = \frac{\exp(i\sqrt{\omega^2 + i0} x_{12})}{4\pi x_{12}}, \quad (4)$$

$G(\varepsilon)$ is the Dirac-Coulomb Green function defined by $G(\varepsilon) = [\varepsilon - \mathcal{H}(1 - i0)]^{-1}$, with \mathcal{H} being the Dirac Coulomb Hamiltonian, and $x_{12} = |\mathbf{x}_1 - \mathbf{x}_2|$. The vertex function Λ^μ is defined as

$$\begin{aligned} \Lambda^\mu(\varepsilon_a - \omega_1, \varepsilon_a) &= 2i\alpha \gamma^0 \int_{-\infty}^{\infty} d\omega_2 D(\omega_2, x_{24}) \alpha_\nu \\ &\times G(\varepsilon_a - \omega_1 - \omega_2) \alpha^\mu G(\varepsilon_a - \omega_2) \alpha^\nu. \end{aligned} \quad (5)$$

The contribution induced by the diagram in Figure 1c will be referred to as the *nested* term. It reads

$$\begin{aligned} \Delta E_N &= 2i\alpha \int_{-\infty}^{\infty} d\omega_1 \int d\mathbf{x}_1 \dots d\mathbf{x}_4 D(\omega_1, x_{14}) \psi_a^\dagger(\mathbf{x}_1) \\ &\times \alpha_\mu G(\varepsilon_a - \omega_1) \gamma^0 \tilde{\Sigma}(\varepsilon_a - \omega_1) \\ &\times G(\varepsilon_a - \omega_1) \alpha^\mu \psi_a(\mathbf{x}_4) - \delta m_N, \end{aligned} \quad (6)$$

where δm_N denotes the mass counterterm.

The general analysis [18] shows that the sum of the reducible, the overlapping, and the nested terms is finite. However, the individual contributions are divergent both in the ultraviolet and the infrared regions of virtual photon energies. In order to make all contributions explicitly finite and suitable for a numerical evaluation, a careful rearrangement of individual parts is required. This rearrangement is discussed in detail in reference [18] and will not be repeated here. The general idea is that the bound electron propagators in the loops are expanded in terms of the interaction with the binding field and the resulting contributions are grouped together into three large classes: (i) the part calculated in coordinate space, conventionally termed the M term and denoted by ΔE_M , (ii) the part calculated in momentum space (the F term ΔE_F), and (iii) the part calculated in the mixed coordinate-momentum representation (the P term ΔE_P),

$$\Delta E_{\text{red}} + \Delta E_O + \Delta E_N = \Delta E_M + \Delta E_F + \Delta E_P. \quad (7)$$

All the three terms can be made explicitly finite and calculated separately. The calculational technique is completely different for each term. In the present investigation, we concentrate on the P term, as the scheme of evaluation of the other two was described in detail in reference [18] and has not been changed significantly since that work.

3 P term: basic formulas

The Feynman diagrams contributing to the P term are shown in Figure 2. They arise from the diagrams in Figure 1 when the bound-electron propagators in the loops are expanded in terms of the interaction with the binding field. The characteristic feature of the diagrams in Figure 2 is that the ultraviolet divergences in them originate from the one-loop subgraphs only. The divergent subgraphs are covariantly regularized and calculated in momentum space, whereas the remaining part of the diagrams does not need any regularization and is evaluated in coordinate space.

It should be mentioned that the necessity of calculation of Feynman diagrams in the mixed coordinate-momentum representation is a distinctive feature of the two-loop effects treated to all orders in the parameter $Z\alpha$. So, the P term has no analog either in the one-loop calculations or, to the best of our knowledge, in any other previous calculations. (All other two-loop effects evaluated to all orders in $Z\alpha$ were effectively reduced to one-loop contributions, see the recent study [22] and references therein.) For the first time the P term was calculated in reference [16] with help of a finite basis set representation of the spectrum of the Dirac equation. In the present investigation we report a different technique based on the analytical representation of the Green function in terms of the Whittaker functions.

As shown in Figure 2, the P term is represented by a sum of five terms,

$$\Delta E_P = \Delta E_{P,a} + \Delta E_{P,b} + \Delta E_{P,c} + \Delta E_{P,d} + \Delta E_{P,e}, \quad (8)$$

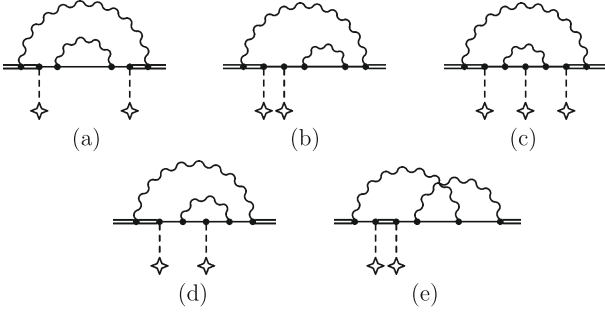


Fig. 2. The P term. The single line represents the free electron propagator. The dashed line with a cross indicates the interaction with the Coulomb field of the nucleus.

each of which refers to the corresponding diagram. In order to make the individual terms finite, we assume that the one-loop subgraphs are represented by the renormalized operators and that the infrared reference-state singularities are removed by the minimal subtractions. It can be explicitly checked that such definition of the P term is equivalent to the definition of reference [18], so that the present numerical results are directly comparable with those of the previous work.

The contribution of the diagram in Figure 2a is given by

$$\begin{aligned} \Delta E_{P,a} = & 2i\alpha \int_{-\infty}^{\infty} d\omega \int \frac{d\mathbf{p}}{(2\pi)^3} \int d\mathbf{x}_1 d\mathbf{x}_2 D(\omega, x_{12}) \\ & \times \psi_a^\dagger(\mathbf{x}_1) \alpha_\mu \left[G_V(E, \mathbf{x}_1, \mathbf{p}) S_1(E, \mathbf{p}) G_V(E, \mathbf{p}, \mathbf{x}_2) \right. \\ & \left. - G_V^{(a)}(E, \mathbf{x}_1, \mathbf{p}) S_1(\varepsilon_a, \mathbf{p}) G_V^{(a)}(E, \mathbf{p}, \mathbf{x}_2) \right] \alpha^\mu \psi_a(\mathbf{x}_2), \quad (9) \end{aligned}$$

where $E = \varepsilon_a - \omega$,

$$S_1(\varepsilon, \mathbf{p}) = \frac{1}{\gamma^0 \varepsilon - \boldsymbol{\gamma} \cdot \mathbf{p} - m} \Sigma_R^{(0)}(\varepsilon, \mathbf{p}) \frac{1}{\gamma^0 \varepsilon - \boldsymbol{\gamma} \cdot \mathbf{p} - m}, \quad (10)$$

$\Sigma_R^{(0)}$ is the renormalized free self-energy operator (see Ref. [18] for its definition and explicit representations), and the function G_V is the Fourier transform of the product of the Green function G and the Coulomb potential $V_C(x) = -Z\alpha/x$,

$$G_V(\varepsilon, \mathbf{x}_1, \mathbf{p}) = \int d\mathbf{x}_2 e^{i\mathbf{p} \cdot \mathbf{x}_2} G(\varepsilon, \mathbf{x}_1, \mathbf{x}_2) V_C(\mathbf{x}_2), \quad (11)$$

$$G_V(\varepsilon, \mathbf{p}, \mathbf{x}_2) = \int d\mathbf{x}_1 e^{-i\mathbf{p} \cdot \mathbf{x}_1} V_C(\mathbf{x}_1) G(\varepsilon, \mathbf{x}_1, \mathbf{x}_2). \quad (12)$$

The second term in the brackets of equation (9) removes the reference-state singularity present in the first term. The definition of the function $G_V^{(a)}$ is obtained from equations (11) and (12) by the substitution $G \rightarrow G^{(a)}$, where $G^{(a)}$ is the reference-state part of the electron propagator defined by

$$G^{(a)}(\varepsilon, \mathbf{x}_1, \mathbf{x}_2) = \sum_{\mu_{a'}} \frac{\psi_{a'}(\mathbf{x}_1) \psi_{a'}^\dagger(\mathbf{x}_2)}{\varepsilon - \varepsilon_a + i0}. \quad (13)$$

Here, $\psi_{a'}$ denotes the virtual electron state of the same energy and of the same parity as the reference state and $\mu_{a'}$ is its angular momentum projection.

The contribution of the diagram in Figure 2b is given by (with the combinatorial factor of 2)

$$\begin{aligned} \Delta E_{P,b} = & 4i\alpha \int_{-\infty}^{\infty} d\omega \int \frac{d\mathbf{p}}{(2\pi)^3} \int d\mathbf{x}_1 d\mathbf{x}_2 D(\omega, x_{12}) \\ & \times \psi_a^\dagger(\mathbf{x}_1) \alpha_\mu \left[G_V(E, \mathbf{x}_1, \mathbf{p}) - G_V^{(0)}(E, \mathbf{x}_1, \mathbf{p}) \right] \\ & \times \mathcal{S}_2(E, \mathbf{p}) G^{(0)}(E, \mathbf{p}, \mathbf{x}_2) \alpha^\mu \psi_a(\mathbf{x}_2), \quad (14) \end{aligned}$$

where

$$\mathcal{S}_2(\varepsilon, \mathbf{p}) = \frac{1}{\gamma^0 \varepsilon - \boldsymbol{\gamma} \cdot \mathbf{p} - m} \Sigma_R^{(0)}(\varepsilon, \mathbf{p}), \quad (15)$$

$G^{(0)}$ is the free Dirac Green function, and the function $G_V^{(0)}$ is defined by equations (11) and (12) after the substitution $G \rightarrow G^{(0)}$.

The contribution of the diagram in Figure 2c is

$$\begin{aligned} \Delta E_{P,c} = & 2i\alpha \int_{-\infty}^{\infty} d\omega \int \frac{d\mathbf{p}_1}{(2\pi)^3} \frac{d\mathbf{p}_2}{(2\pi)^3} \int d\mathbf{x}_1 d\mathbf{x}_2 \\ & \times D(\omega, x_{12}) V_C(\mathbf{q}) \psi_a^\dagger(\mathbf{x}_1) \alpha_\mu \\ & \times \left[G_V(E, \mathbf{x}_1, \mathbf{p}_1) \mathcal{G}_1(E, \mathbf{p}_1, \mathbf{p}_2) G_V(E, \mathbf{p}_2, \mathbf{x}_2) \right. \\ & \left. - G_V^{(a)}(E, \mathbf{x}_1, \mathbf{p}_1) \mathcal{G}_1(\varepsilon_a, \mathbf{p}_1, \mathbf{p}_2) G_V^{(a)}(E, \mathbf{p}_2, \mathbf{x}_2) \right] \\ & \times \alpha^\mu \psi_a(\mathbf{x}_2), \quad (16) \end{aligned}$$

where $V_C(\mathbf{q}) = -4\pi Z\alpha/q^2$ is the Coulomb potential in momentum space, $\mathbf{q} = \mathbf{p}_1 - \mathbf{p}_2$,

$$\begin{aligned} \mathcal{G}_1(\varepsilon, \mathbf{p}_1, \mathbf{p}_2) = & \frac{1}{\gamma^0 \varepsilon - \boldsymbol{\gamma} \cdot \mathbf{p}_1 - m} \\ & \times \Gamma_R^0(\varepsilon, \mathbf{p}_1; \varepsilon, \mathbf{p}_2) \frac{1}{\gamma^0 \varepsilon - \boldsymbol{\gamma} \cdot \mathbf{p}_2 - m}, \quad (17) \end{aligned}$$

and Γ_R^0 is the time component of the renormalized free vertex operator Γ_R^μ (its explicit representation can be found in Ref. [18]).

The contribution of the diagram in Figure 2d is given by (with the combinatorial factor of 2)

$$\begin{aligned} \Delta E_{P,d} = & 4i\alpha \int_{-\infty}^{\infty} d\omega \int \frac{d\mathbf{p}_1}{(2\pi)^3} \frac{d\mathbf{p}_2}{(2\pi)^3} \int d\mathbf{x}_1 d\mathbf{x}_2 \\ & \times D(\omega, x_{12}) V_C(\mathbf{q}) \psi_a^\dagger(\mathbf{x}_1) \alpha_\mu G_V(E, \mathbf{x}_1, \mathbf{p}_1) \\ & \times \mathcal{G}_2(E, \mathbf{p}_1, \mathbf{p}_2) G^{(0)}(E, \mathbf{p}_2, \mathbf{x}_2) \alpha^\mu \psi_a(\mathbf{x}_2), \quad (18) \end{aligned}$$

where

$$\mathcal{G}_2(\varepsilon, \mathbf{p}_1, \mathbf{p}_2) = \frac{1}{\gamma^0 \varepsilon - \boldsymbol{\gamma} \cdot \mathbf{p}_1 - m} \Gamma_R^0(\varepsilon, \mathbf{p}_1; \varepsilon, \mathbf{p}_2). \quad (19)$$

The contribution of the diagram in Figure 2e can be written as (with the combinatorial factor of 2)

$$\begin{aligned} \Delta E_{P,e} &= -4i\alpha \int_{-\infty}^{\infty} d\omega \int \frac{d\mathbf{p}_1}{(2\pi)^3} \frac{d\mathbf{p}_2}{(2\pi)^3} \int dz \\ &\times \frac{\exp(-i\mathbf{q} \cdot \mathbf{z})}{\omega^2 - \mathbf{q}^2 + i0} \psi_a^\dagger(\mathbf{z}) \alpha_\mu \\ &\times \left[G_V(E, \mathbf{z}, \mathbf{p}_1) - G_V^{(0)}(E, \mathbf{z}, \mathbf{p}_1) \right] \\ &\times \frac{1}{\gamma^0 E - \boldsymbol{\gamma} \cdot \mathbf{p}_1 - m} \Gamma_R^\mu(E, \mathbf{p}_1; \varepsilon_a, \mathbf{p}_2) \psi_a(\mathbf{p}_2). \end{aligned} \quad (20)$$

4 Calculation

The main problem of the evaluation of the P term is connected with the fact that the regularization of ultraviolet divergences in the one-loop subgraphs is carried out in momentum space, while the bound-electron propagators are most easily evaluated in coordinate space. As a result, the expressions listed in the previous section contain the Fourier transform of the product of the Dirac Coulomb Green functions G with the Coulomb potential V_C over one of the radial arguments, see equations (11) and (12). Since we were not able to find a satisfactory analytical representation for such an object, the only possible way was to evaluate the Fourier transform integral numerically. This entails numerous numerical integrations of rapidly oscillating functions, which may make the computations prohibitively expensive, unless great care is taken in choosing the optimal calculational approach.

In the previous investigations [16–18], the P term was calculated with help of a finite basis set for the Dirac equation. The advantage of the basis-set methods is that they represent the Dirac Green function as a continuous function of the radial arguments (for any finite size of the basis), whereas the exact Green function is discontinuous when the two radial arguments are equal. The usage of a finite basis set allows one to perform the Fourier transform of the Green function over one radial variable independently of the other. However, the convergence with respect to the size of the basis appears to be the limiting factor for the accuracy of the calculations in that case. In the present investigation, we set up a different calculational approach based on the analytical representation of the Green function. Technical details of evaluation of the Dirac Coulomb Green function in the mixed coordinate-momentum representation are described in Appendix A. The corresponding formulas for the free Dirac Green function are summarized in Appendix B.

4.1 Nested diagrams

In this subsection, we address the diagrams in Figures 2a–2d and outline the major steps required to make the basic formulas suitable for a numerical evaluation.

The integrations over the angular variables ($\hat{\mathbf{x}}_1$, $\hat{\mathbf{x}}_2$, and $\hat{\mathbf{p}}$ in Eqs. (9) and (14) and $\hat{\mathbf{x}}_1$, $\hat{\mathbf{x}}_2$, $\hat{\mathbf{p}}_1$, and $\hat{\mathbf{p}}_2$ in Eqs. (16) and (18), where $\hat{\mathbf{x}} = \mathbf{x}/|\mathbf{x}|$) are relatively simple. We employ the fact that the matrix elements of the operators $\mathcal{S}_{1,2}$ and $\mathcal{G}_{1,2}$ with the Dirac wave functions are (i) diagonal with respect to the angular momentum quantum number κ and the angular momentum projection μ and (ii) do not depend on μ :

$$\langle \kappa\mu | \mathcal{S}_i | \kappa'\mu' \rangle = \delta_{\kappa,\kappa'} \delta_{\mu,\mu'} \langle \kappa | \mathcal{S}_i | \kappa \rangle, \quad (21)$$

$$\langle \kappa\mu | \mathcal{G}_i V_C | \kappa'\mu' \rangle = \delta_{\kappa,\kappa'} \delta_{\mu,\mu'} \langle \kappa | \mathcal{G}_i V_C | \kappa \rangle. \quad (22)$$

As a result, the integrations over $\hat{\mathbf{p}}$ in equations (9) and (14) and $\hat{\mathbf{p}}_1$ and $\hat{\mathbf{p}}_2$ in equations (16) and (18) are exactly the same as for the zero- and one-potential parts of the one-loop self-energy correction, see reference [23] for details. The integrations over $\hat{\mathbf{x}}_1$ and $\hat{\mathbf{x}}_2$ are the same as for the many-potential part of the one-loop self-energy correction.

As illustrated in reference [23], the integrations over $\hat{\mathbf{p}}_1$ and $\hat{\mathbf{p}}_2$ in equations (16) and (18) can be easily reduced to a single integral over $\xi = \hat{\mathbf{p}}_1 \cdot \hat{\mathbf{p}}_2$, which needs to be evaluated numerically. The calculation is complicated by the presence of an integrable Coulomb singularity ($\sim 1/q^2$, $q = |\mathbf{p}_1 - \mathbf{p}_2|$). This singularity is removed in two steps. First, the change of the integration variable $\xi \rightarrow q$ weakens it to $\sim 1/q$. The remaining singularity is removed by subtraction of the vertex function with the equal arguments,

$$\Gamma_R^0(p_1, p_2) \rightarrow \Gamma_R^0(p_1, p_2) - \frac{1}{2} [\Gamma_R^0(p_1, p_1) + \Gamma_R^0(p_2, p_2)]. \quad (23)$$

The vertex operator with two equal arguments is related to the free self-energy operator by the Ward identity:

$$\Gamma_R^0(p, p) = -\frac{\partial}{\partial p^0} \Sigma_R^{(0)}(p). \quad (24)$$

In the subtracted terms, the Coulomb singularity is easily integrated out by using identities obtained from the definition of the Dirac Coulomb Green function, e.g.,

$$\begin{aligned} \int \frac{d\mathbf{p}_2}{(2\pi)^3} V_C(\mathbf{q}) \frac{1}{\gamma^0 E - \boldsymbol{\gamma} \cdot \mathbf{p}_2 - m} G_V(E, \mathbf{p}_2, \mathbf{x}_2) = \\ G_V(E, \mathbf{p}_1, \mathbf{x}_2) - G_V^{(0)}(E, \mathbf{p}_1, \mathbf{x}_2). \end{aligned} \quad (25)$$

Finally, we change the contour of the integration over the virtual photon energy ω in equations (9), (14), (16), and (18) from $(-\infty, \infty)$ to a new contour C_{LH} , whose main part is parallel to the imaginary axis. The contour C_{LH} consists of the low-energy C_L and the high-energy C_H parts. The low-energy part extends over $(\Delta - i0, -i0)$ on the lower bank of the cut of the photon propagator and over $(i0, \Delta + i0)$ on the upper bank of the cut, with the parameter Δ fixed by $\Delta = Z\alpha\varepsilon_a$. The high-energy part consists of two intervals, $(\Delta + i0, \Delta + i\infty)$ and $(\Delta - i0, \Delta - i\infty)$. The contour C_{LH} differs from the one used by Mohr [12,13] only by the choice of the breaking point Δ (the value $\Delta = \varepsilon_a$ was employed in that work).

In our previous calculations we used the contour that extended along the imaginary axis (which corresponds to the choice of $\Delta = 0$). The contour C_{LH} is more convenient for the numerical evaluation. Firstly, there is no pole contributions originating from the reference-state part of the electron propagators. Secondly and more importantly, the photon propagator on the low-energy part of the contour involves $\sin(\omega x_{12})$, which suppresses small denominators due to the virtual bound states and leads to a smooth behaviour of the integrand for small ω .

In the present investigation, we are concerned with the reference state being the ground state only. In this case, no pole contributions appears for the contour C_{LH} . For the excited reference states, however, there are single and double poles on the low-energy part of the contour, which arise from the intermediate states bound more deeply than the reference state. These poles require a separate treatment or a deformation of the integration contour into the complex plane.

4.2 Overlapping diagram

In this subsection we address the overlapping diagram shown in Figure 2e, whose expression is given by equation (20). The angular integration in this expression is rather involved and will be considered in detail.

In order to perform the integration over $\hat{\mathbf{z}}$, we expand the exponent into the spherical waves,

$$e^{-i\mathbf{q}\cdot\mathbf{z}} = 4\pi \sum_{LM} i^{-L} j_L(qz) Y_{LM}(\hat{\mathbf{q}}) Y_{LM}^*(\hat{\mathbf{z}}), \quad (26)$$

where j_L is the spherical Bessel function and Y_{LM} is the spherical harmonics. The time component ($\mu = 0$) of the $\hat{\mathbf{z}}$ integration is immediately evaluated in terms of the basic integrals of the form

$$\int d\hat{\mathbf{z}} \chi_{\kappa_b\mu_b}^\dagger(\hat{\mathbf{z}}) Y_{LM}(\hat{\mathbf{z}}) \chi_{\kappa_a\mu_a}(\hat{\mathbf{z}}) = s_{LM}^{ba} \langle \kappa_b || \mathbf{C}^{(L)} || \kappa_a \rangle, \quad (27)$$

where $\chi_{\kappa\mu}(\hat{\mathbf{z}})$ are the Dirac spin-angular spinors [24], $\mathbf{C}^{(L)}$ is the spherical tensor with components $\mathbf{C}_M^{(L)}(\hat{\mathbf{r}}) = \sqrt{4\pi/(2L+1)} Y_{LM}(\hat{\mathbf{r}})$, $\langle || \cdots || \rangle$ denotes the reduced matrix element, and

$$s_{LM}^{ba} = \frac{(-1)^{j_a - \mu_a}}{\sqrt{4\pi}} C_{j_b\mu_b, j_a - \mu_a}^{LM}, \quad (28)$$

with $C_{j_1 m_1, j_2 m_2}^{j m}$ being the Clebsch-Gordan coefficient.

The vector components ($\mu = 1, 2, 3$) of the $\hat{\mathbf{z}}$ integration are calculated after expanding the integrand in terms of the vector spherical harmonics \mathbf{Y}_{JLM} [25,26],

$$\chi_{\kappa_b\mu_b}^\dagger(\hat{\mathbf{z}}) \boldsymbol{\sigma} \chi_{\kappa_a\mu_a}(\hat{\mathbf{z}}) = \sum_{JLM} s_{JM}^{ab} S_{JL}(\kappa_b, \kappa_a) \mathbf{Y}_{JLM}(\hat{\mathbf{z}}), \quad (29)$$

where $\boldsymbol{\sigma}$ is a vector incorporating Pauli matrices. The coefficients S_{JL} are given by

$$S_{JJ+1}(\kappa_a, \kappa_b) = \sqrt{\frac{J+1}{2J+1}} \left(1 + \frac{\kappa_a + \kappa_b}{J+1} \right) \times \langle -\kappa_b || \mathbf{C}^{(J)} || \kappa_a \rangle, \quad (30)$$

$$S_{JJ}(\kappa_a, \kappa_b) = \frac{\kappa_a - \kappa_b}{\sqrt{J(J+1)}} \langle \kappa_b || \mathbf{C}^{(J)} || \kappa_a \rangle, \quad (31)$$

$$S_{JJ-1}(\kappa_a, \kappa_b) = \sqrt{\frac{J}{2J+1}} \left(-1 + \frac{\kappa_a + \kappa_b}{J} \right) \times \langle -\kappa_b || \mathbf{C}^{(J)} || \kappa_a \rangle. \quad (32)$$

For $J = 0$, the only non-vanishing coefficient is S_{01} .

We now turn to the evaluation of the integrals over $\hat{\mathbf{p}}_1$ and $\hat{\mathbf{p}}_2$ in equation (20). The aim is to integrate out all angular variables except $\xi = \hat{\mathbf{p}}_1 \cdot \hat{\mathbf{p}}_2$. To this end, we examine the angular structures encountered in the integrand. The time component of the vertex operator sandwiched between the Dirac wave functions involves two independent angular structures, which are identified by

$$\begin{aligned} \psi_n^\dagger(\mathbf{p}_1) \frac{1}{\gamma^0 E - \boldsymbol{\gamma} \cdot \mathbf{p}_1 - m} \Gamma_R^0(E, \mathbf{p}_1; \varepsilon_a, \mathbf{p}_2) \psi_a(\mathbf{p}_2) = \\ \frac{\alpha}{4\pi} i^{l_n - l_a} \left\{ [g_n \mathcal{F}_{1g} + f_n \mathcal{F}_{1f}] \chi_{\kappa_n\mu_n}^\dagger(\hat{\mathbf{p}}_1) \chi_{\kappa_a\mu_a}(\hat{\mathbf{p}}_2) \right. \\ \left. + [g_n \mathcal{F}_{2g} + f_n \mathcal{F}_{2f}] \chi_{-\kappa_n\mu_n}^\dagger(\hat{\mathbf{p}}_1) \chi_{-\kappa_a\mu_a}(\hat{\mathbf{p}}_2) \right\}, \quad (33) \end{aligned}$$

where $g_n \equiv g_n(p_1)$ and $f_n \equiv f_n(p_1)$ are the upper and the lower radial components of the Dirac wave function ψ_n and \mathcal{F}_i are scalar functions $\mathcal{F}_i \equiv \mathcal{F}_i(E, \varepsilon_a, p_1, p_2, q)$, with $p_1 = |\mathbf{p}_1|$, $p_2 = |\mathbf{p}_2|$, and $q = |\mathbf{q}|$. The vector part of the vertex operator induces six angular structures,

$$\begin{aligned} \psi_n^\dagger(\mathbf{p}_1) \frac{1}{\gamma^0 E - \boldsymbol{\gamma} \cdot \mathbf{p}_1 - m} \boldsymbol{\Gamma}_R(E, \mathbf{p}_1; \varepsilon_a, \mathbf{p}_2) \psi_a(\mathbf{p}_2) = \\ \frac{\alpha}{4\pi} i^{l_n - l_a} \left\{ [g_n \mathcal{R}_{1g} + f_n \mathcal{R}_{1f}] \chi_{\kappa_n\mu_n}^\dagger(\hat{\mathbf{p}}_1) \boldsymbol{\sigma} \chi_{-\kappa_a\mu_a}(\hat{\mathbf{p}}_2) \right. \\ + [g_n \mathcal{R}_{2g} + f_n \mathcal{R}_{2f}] \chi_{-\kappa_n\mu_n}^\dagger(\hat{\mathbf{p}}_1) \boldsymbol{\sigma} \chi_{\kappa_a\mu_a}(\hat{\mathbf{p}}_2) \\ + [g_n \mathcal{R}_{3g} + f_n \mathcal{R}_{3f}] \mathbf{p}_1 \chi_{\kappa_n\mu_n}^\dagger(\hat{\mathbf{p}}_1) \chi_{\kappa_a\mu_a}(\hat{\mathbf{p}}_2) \\ + [g_n \mathcal{R}_{4g} + f_n \mathcal{R}_{4f}] \mathbf{p}_2 \chi_{\kappa_n\mu_n}^\dagger(\hat{\mathbf{p}}_1) \chi_{\kappa_a\mu_a}(\hat{\mathbf{p}}_2) \\ + [g_n \mathcal{R}_{5g} + f_n \mathcal{R}_{5f}] \mathbf{p}_1 \chi_{-\kappa_n\mu_n}^\dagger(\hat{\mathbf{p}}_1) \chi_{-\kappa_a\mu_a}(\hat{\mathbf{p}}_2) \\ \left. + [g_n \mathcal{R}_{6g} + f_n \mathcal{R}_{6f}] \mathbf{p}_2 \chi_{-\kappa_n\mu_n}^\dagger(\hat{\mathbf{p}}_1) \chi_{-\kappa_a\mu_a}(\hat{\mathbf{p}}_2) \right\}, \quad (34) \end{aligned}$$

where $\mathcal{R}_i \equiv \mathcal{R}_i(E, \varepsilon_a, p_1, p_2, q)$. The functions \mathcal{F}_i and \mathcal{R}_i can be straightforwardly obtained from formulas in Appendix A of reference [27].

Using equations (33) and (34), it is possible to parameterize the angular structure of the integrand of equation (20) by four basic angular factors t_{κ_1, κ_2} , $s_{\kappa_1, \kappa_2}^\sigma$, $s_{\kappa_1, \kappa_2}^{p_1}$, and $s_{\kappa_1, \kappa_2}^{p_2}$ defined as

$$t_{\kappa_n, \kappa_a}(J) = \sum_{\mu_n M} s_{JM}^{na} \chi_{\kappa_n \mu_n}^\dagger(\hat{\mathbf{p}}_1) Y_{JM}(\hat{\mathbf{q}}) \chi_{\kappa_a \mu_a}(\hat{\mathbf{p}}_2), \quad (35)$$

$$s_{\kappa_n, \kappa_a}^\sigma(JL) = \sum_{\mu_n M} s_{JM}^{na} \chi_{\kappa_n \mu_n}^\dagger(\hat{\mathbf{p}}_1) \boldsymbol{\sigma} \cdot \mathbf{Y}_{JLM}(\hat{\mathbf{q}}) \chi_{\kappa_a \mu_a}(\hat{\mathbf{p}}_2), \quad (36)$$

$$s_{\kappa_n, \kappa_a}^{p_i}(JL) = \sum_{\mu_n M} s_{JM}^{na} \chi_{\kappa_n \mu_n}^\dagger(\hat{\mathbf{p}}_1) \hat{\mathbf{p}}_i \cdot \mathbf{Y}_{JLM}(\hat{\mathbf{q}}) \chi_{\kappa_a \mu_a}(\hat{\mathbf{p}}_2). \quad (37)$$

By an explicit evaluation with help of formulas from reference [26], one can show that the above angular factors are the functions of p_1 , p_2 , and q only (or, in other words, that they depend on the angular variables only through ξ). This statement allows us to integrate out all angles in equation (20) except ξ . The calculation of angular factors is described in Appendix C.

For a numerical evaluation of equation (20), we need to deform the contour of the ω integration. In this case (in contrast to the nested contributions), we find it convenient just to rotate the integration contour to the imaginary axis, $\omega \rightarrow i\omega$. This leads to appearance of the pole contribution. So,

$$\Delta E_{P,e} = \Delta E_{P,e}^{\text{Im}} + \Delta E_{P,e}^{\text{pole}}, \quad (38)$$

where $\Delta E_{P,e}^{\text{Im}}$ is the contribution of the integral along the imaginary axis and $\Delta E_{P,e}^{\text{pole}}$ is the pole contribution.

The final result after the angular integrations and the rotation of the contour is

$$\begin{aligned} \Delta E_{P,e}^{\text{Im}} = & \frac{\alpha^2}{\pi^4} \text{Re} \sum_{\kappa_n} \int_0^\infty d\omega \int_0^\infty dp_1 dq \int_{|p_1-q|}^{p_1+q} dp_2 \frac{q p_1 p_2}{-\omega^2 - q^2} \\ & \times \int_0^\infty dz z^2 \left\{ \sum_J (-1)^{k_1} j_J(qz) \langle \kappa_n | | \mathbf{C}^{(J)} | | \kappa_a \rangle \right. \\ & \times \left[(g_a \tilde{G}_{V_{\kappa_n}}^{11} + f_a \tilde{G}_{V_{\kappa_n}}^{21}) \mathcal{F}_g + (g_a \tilde{G}_{V_{\kappa_n}}^{12} + f_a \tilde{G}_{V_{\kappa_n}}^{22}) \mathcal{F}_f \right] \\ & - \sum_{JL} (-1)^{k_2} j_L(qz) \left([g_a \tilde{G}_{V_{\kappa_n}}^{21} S_{JL}(\kappa_a, -\kappa_n) \right. \\ & \quad \left. - f_a \tilde{G}_{V_{\kappa_n}}^{11} S_{JL}(-\kappa_a, \kappa_n)] \mathcal{R}_g \right. \\ & \left. + [g_a \tilde{G}_{V_{\kappa_n}}^{22} S_{JL}(\kappa_a, -\kappa_n) - f_a \tilde{G}_{V_{\kappa_n}}^{12} S_{JL}(-\kappa_a, \kappa_n)] \mathcal{R}_f \right) \left. \right\}, \quad (39) \end{aligned}$$

where $k_1 = (J - l_n + l_a)/2$, $k_2 = (L - l_n + l_a - 1)/2$, $l_n = |\kappa_n + 1/2| - 1/2$, $g_a \equiv g_a(z)$ and $f_a \equiv f_a(z)$ are the

radial components of the reference-state wave function, and $\tilde{G}_{V_{\kappa_n}}^{ij}$ stand for the difference of the radial components of the Coulomb Green function (times V_C) and the free Green function (times V_C),

$$\tilde{G}_{V_{\kappa_n}}^{ij} \equiv G_{V_{\kappa_n}}^{ij}(\varepsilon_a - i\omega, z, p_1) - G_{V_{\kappa_n}}^{(0)ij}(\varepsilon_a - i\omega, z, p_1).$$

The angular functions in equation (39) are defined by

$$\mathcal{F}_g = \mathcal{F}_{1g} t_{\kappa_n, \kappa_a}(J) + \mathcal{F}_{2g} t_{-\kappa_n, -\kappa_a}(J), \quad (40)$$

$$\begin{aligned} \mathcal{R}_g = & \mathcal{R}_{1g} s_{\kappa_n, -\kappa_a}^\sigma(JL) + \mathcal{R}_{2g} s_{-\kappa_n, \kappa_a}^\sigma(JL) \\ & + p_1 \mathcal{R}_{3g} s_{\kappa_n, \kappa_a}^{p_1}(JL) + p_2 \mathcal{R}_{4g} s_{\kappa_n, \kappa_a}^{p_2}(JL) \\ & + p_1 \mathcal{R}_{5g} s_{-\kappa_n, -\kappa_a}^{p_1}(JL) + p_2 \mathcal{R}_{6g} s_{-\kappa_n, -\kappa_a}^{p_2}(JL), \quad (41) \end{aligned}$$

and the same for the \mathcal{F}_f and \mathcal{R}_f functions.

The pole contribution $\Delta E_{P,e}^{\text{pole}}$ is obtained from equation (39) by the following substitution (valid for a being the ground state),

$$\tilde{G}_{V_{\kappa_n}}^{ij} \rightarrow -\frac{\pi}{2} \delta_{\kappa_n \kappa_a} \delta(\omega) \phi_a^i(z) \phi_{V_a}^j(p_1), \quad (42)$$

where $\phi_a^1(z) = g_a(z)$, $\phi_a^2(z) = f_a(z)$, and $\phi_{V_a}^j(p)$ is the Fourier transform of the product $\phi_a^i(x) V_C(x)$.

A useful check of the angular-momentum algebra consists in making the substitution $\Gamma_R^\mu(E, \mathbf{p}_1; \varepsilon_a, \mathbf{p}_2) \rightarrow \gamma^\mu$ in equation (20). The result is a one-loop self-energy contribution which can be calculated independently in the coordinate representation.

4.3 Numerical evaluation

We start our discussion of the numerical evaluation of the P term with $\Delta E_{P,a}$ and $\Delta E_{P,b}$ given by equations (9) and (14), respectively. These are the two simplest contributions. After carrying out integrations over the angular variables as described in Section 4.1, five integrations remain to be calculated numerically, namely those over ω , p , x_1 , and x_2 and the Bessel transform integral implicitly present in the Green function.

The radial integrations over x_1 and x_2 have to be organized in such a way as to avoid unnecessary recalculation of the Bessel transform integrals, as discussed in Appendix A. To this end, we set up a radial grid $\{x_{i,j,k}\}$ as follows. The first-level elements $x_{i,0,0}$ are given by

$$x_{i,0,0} = \rho_0 \frac{1 - t_i^2}{t_i^2}, \quad (43)$$

where ρ_0 is a parameter adjusted empirically, the variable t_i is uniformly distributed over the interval $(t_{\min}, 1)$, and a small value of $t_{\min} > 0$ cuts off the radial integrations at large distances. The second-level elements $x_{i,j,0}$

represent the Gauss-Legendre quadratures on the interval $(x_{i,0,0}, x_{i+1,0,0})$. The third-level elements $x_{i,j,k}$ represent the Gauss-Legendre quadratures on the interval $(x_{i,j,0}, x_{i,j+1,0})$. In the result, we obtain an ordered three-level radial grid. To perform the radial integrations over x_1 and x_2 , it is sufficient to know the integrand on this grid only.

The general scheme of the evaluation of $\Delta E_{P,a}$ is as follows. For fixed values of κ , ω , and p , we set up the radial grid $\{x_{i,j,k}\}$. On this radial grid, we store the components of the Dirac Green function $\phi_\kappa^0(E, x)$ and $\phi_\kappa^\infty(E, x)$ (see Eqs. (A.3) and (A.4)), the Bessel transform functions $\psi_\kappa^0(E, p; x)$ and $\psi_\kappa^\infty(E, p; x)$ (see Eqs. (A.9) and (A.10)), and the other functions required for the evaluation of the integrand (the radial part of the photon propagator, the reference-state wave function, etc.). After that, the radial integrations are performed simply by summing up the stored numerical values. Next, we perform the integration over p , then the one over ω , and finally, the summation over κ .

The most expensive part of the calculation is the evaluation of the Bessel transform integrals. In order to control the accuracy of numerical integrations, one needs an efficient procedure for calculating the transforms for various momenta, including ones as large as 10^6 . In our calculations, we used the Gauss-Legendre integration quadratures in the region where the argument of the Bessel function is of about unity or smaller. Outside this region, the spherical Bessel function was expressed as a combination of the sine and cosine functions. The numerical evaluation of the sine and cosine transform was performed with help of routines of the NAG Fortran library.

The scheme described above works well for the $\Delta E_{P,a}$ contribution but turns out to be not sufficiently effective for $\Delta E_{P,b}$, leading to a slow convergence of the radial integrations with respect to the number of integration points. This is because the free Green function $G^{(0)}(\varepsilon, \mathbf{x}, \mathbf{p})$ contains a Bessel function (see Eq. (B.5)), which oscillates rapidly in the high-momenta region. This problem was solved by observing that the integral over x_2 in equation (14) has a structure similar to $\psi_\kappa(E, p; x_1)$, i.e., it is essentially a Bessel transform over the intervals $(0, x_1)$ and (x_1, ∞) . We thus perform the integration over x_2 in equation (14) by means of the same approach as used in the evaluation of the Bessel transform functions $\psi_\kappa(E, p; x_1)$. This approach improves the convergence of the radial integrals drastically.

The evaluation of the two remaining nested contributions, $\Delta E_{P,c}$ and $\Delta E_{P,d}$, was performed in full analogy with those discussed above. However, it turned out to be much more time consuming due to a larger number of integrations. Indeed, in place of an integration over p in $\Delta E_{P,a}$ and $\Delta E_{P,b}$, there are now four integrations (those over p_1 , p_2 , and q and the Feynman-parameter integration implicitly present in the vertex operator). Fortunately, the integrations over q and over the Feynman parameter can be carried out independently of the integrations over x_1 and x_2 and thus do not significantly influence the total calculational time. The two integrations over p_1 and p_2 ,

however, lead to a considerable increase of the computational expense (this being about a week of the processor time for each value of Z).

For the overlapping contribution $\Delta E_{P,e}$, there are seven integrations to be performed numerically. Five of them are explicitly written in equation (39), one over the Feynman parameter is implicitly present in the vertex operator, and the last one is the Bessel transform integral in the Green function. The number of nested integrations can be reduced by observing that the integrations over p_2 and over the Feynman parameter can be carried out independently of the integration over z . The calculation is complicated by the fact that the integral over z contains a Bessel function. In order to obtain a stable result for the z integration in the region of large values of qz , we had to interpolate the part of the integrand that multiplies the Bessel function and evaluate the Bessel transform analytically.

5 Results and discussion

The results of our calculation of the P term for the ground state of hydrogen-like ions with $Z \geq 10$ are listed in Table 1. The individual contributions are presented in a way that allows a detailed comparison with the previous calculations. Specifically, the first four columns of Table 1 are directly comparable to the four columns of Table 2 in reference [18]. The previous results listed in the fifth column of Table 1 were obtained in reference [19] for $Z \leq 60$ and in reference [18] for the other Z . The agreement with the previous calculations is very good in most cases, but the present numerical accuracy is significantly higher. A small deviation in the high- Z region is probably due to a difference in the treatment of the nucleus. (In the present work, the point nuclear model is used, whereas the previous investigations [18,19] were conducted with a partial inclusion of the finite nuclear size effect in the P term.)

The uncertainty of the present results is mainly due to the termination of the partial-wave expansion. In our calculation, we included typically 20–30 partial waves and estimated the omitted tail by fitting the data obtained as a function of the cutoff parameter. An extension of the partial-wave summation further than that is rather problematic, since the high partial waves become increasingly difficult to control numerically. At the same time, an extrapolation of the partial wave expansion requires the individual partial-wave expansion terms to be calculated to a relatively high accuracy.

The main motivation of the present investigation was to improve the numerical accuracy of the total two-loop self-energy correction in the region of medium values of Z , in order to get a more reliable extrapolation towards $Z = 0$. To this end, a new approach was developed for the evaluation of the P term, as described above. Besides that, the other parts of the two-loop self-energy correction were reevaluated to a higher accuracy. This was accomplished by the methods described in reference [18], with the increased number of partial waves included and with

Table 1. The P term for the ground state of hydrogen-like ions, in units of $\Delta E/[m\alpha^2(Z\alpha)^4/\pi^2]$.

Z	Figs. (a), (b)	Figs. (c), (d)	Fig. (e)	Total	Previous [18,19]
10	-855.4289 (20)	1265.4550 (50)	-1131.3372 (22)	-721.3111 (58)	-721.34 (12)
12	-486.0740 (20)	744.6950 (50)	-697.6864 (17)	-439.0654 (56)	
15	-239.2533 (15)	384.3590 (30)	-380.3170 (12)	-235.2113 (36)	-235.205 (70)
17	-159.4480 (15)	263.5625 (20)	-268.3945 (12)	-164.2800 (28)	
20	-93.3597 (7)	160.3551 (20)	-169.0247 (10)	-102.0293 (23)	-102.026 (55)
25	-44.1892 (7)	79.9950 (15)	-87.7882 (10)	-51.9824 (19)	
30	-23.8155 (7)	44.8102 (27)	-50.4083 (10)	-29.4135 (30)	-29.410 (25)
40	-9.0138 (4)	17.6061 (2)	-20.1713 (6)	-11.5790 (7)	-11.575 (30)
50	-4.3391 (5)	8.4020 (4)	-9.5506 (4)	-5.4877 (7)	-5.488 (26)
60	-2.4455 (3)	4.5451 (4)	-5.0660 (2)	-2.9664 (5)	-2.970 (18)
70	-1.5203 (2)	2.6716 (1)	-2.9354 (2)	-1.7841 (3)	-1.757 (25)
83	-0.8655 (2)	1.4268 (1)	-1.6307 (1)	-1.0693 (2)	-1.057 (13)
92	-0.5545 (1)	0.9091 (1)	-1.1902 (1)	-0.8356 (2)	-0.812 (10)
100	-0.2990 (2)	0.5426 (1)	-0.9792 (4)	-0.7356 (5)	-0.723 (7)

Table 2. The two-loop self-energy correction for the ground state of hydrogen-like ions, in units of $\Delta E/[m\alpha^2(Z\alpha)^4/\pi^2]$.

Z	LAL	F term	P term	M term	Total	2005 results [19]
10	-0.358	822.138 (5)	-721.311 (6)	-100.297 (35)	0.172 (36)	0.25 (16)
12	-0.417	519.603 (2)	-439.065 (6)	-80.117 (38)	0.004 (38)	
15	-0.495	292.901 (2)	-235.211 (4)	-57.406 (11)	-0.212 (12)	-0.164 (85)
17	-0.541	211.052 (1)	-164.280 (3)	-46.567 (9)	-0.336 (10)	
20	-0.602	136.909 (1)	-102.029 (2)	-34.780 (4)	-0.501 (5)	-0.481 (58)
25	-0.686	74.501 (1)	-51.982 (2)	-22.560 (6)	-0.728 (6)	
30	-0.756	44.728 (1)	-29.414 (3)	-15.468 (3)	-0.910 (5)	-0.903 (26)

denser integration grids. The results were first presented in reference [21].

Table 2 summarizes our results for the total two-loop self-energy correction for the ground state of hydrogen-like ions with the nuclear charge $Z = 10-30$. We observe that the calculational errors of the P term do not influence significantly the errors of the total results, as the main uncertainty is now delivered by the M term. This uncertainty originates both from the dependence of the results on the number of integration points and from the termination of the partial-wave expansions. Since there are two independent partial-wave expansion parameters in the M term (see Ref. [18] for details), the number of expansion terms grows drastically as the cutoff parameter is increased. Because of this, significant extension of the partial-wave summations looks prohibitively expensive at present.

The two-loop self-energy correction for the ground state of hydrogen-like atoms can be conveniently represented in the following form, separating out the known terms of the $Z\alpha$ expansion,

$$\Delta E = m \left(\frac{\alpha}{\pi}\right)^2 (Z\alpha)^4 \left[B_{40} + (Z\alpha) G_{50}(Z) \right], \quad (44)$$

and

$$G_{50}(Z) = B_{50} + (Z\alpha) \left\{ \ln^3[(Z\alpha)^{-2}] B_{63} + \ln^2[(Z\alpha)^{-2}] B_{62} + \ln[(Z\alpha)^{-2}] B_{61} + G_{60}(Z) \right\}, \quad (45)$$

where B_{ij} are the expansion coefficients with the first index corresponding to the power of $Z\alpha$ and the second index, to the power of logarithm, and $G_{ij}(Z)$ are the functions incorporating the corresponding B_{ij} and all higher orders in $Z\alpha$, $G_{ij}(Z) = B_{ij} + Z\alpha(\dots)$. The results for the expansion coefficients are: $B_{40} = 1.409244$ [28], $B_{50} = -24.2668(31)$ [29,30], $B_{63} = -8/27$ [2,31,32], $B_{62} = 16/27 - (16/9) \ln 2$ [2], $B_{61} = 48.388913$ [2,5], and $B_{60} = -61.6(9.2)$ [3].

The functions $G_{ij}(Z)$ inferred from our numerical data are plotted in Figure 3. The visual agreement of our results with the analytical values of the expansion coefficients is very good for B_{40} and B_{50} , but not exactly satisfactory for B_{60} . In order to produce a clearer statement, we need to extrapolate our data towards low values of Z . For this we use a variant of the procedure first employed in reference [33]. The extrapolation towards the required value of $Z = Z_0$ ($= 0$ and 1 in our case) is performed in two steps. First, we apply an (exact) linear fit to each pair of

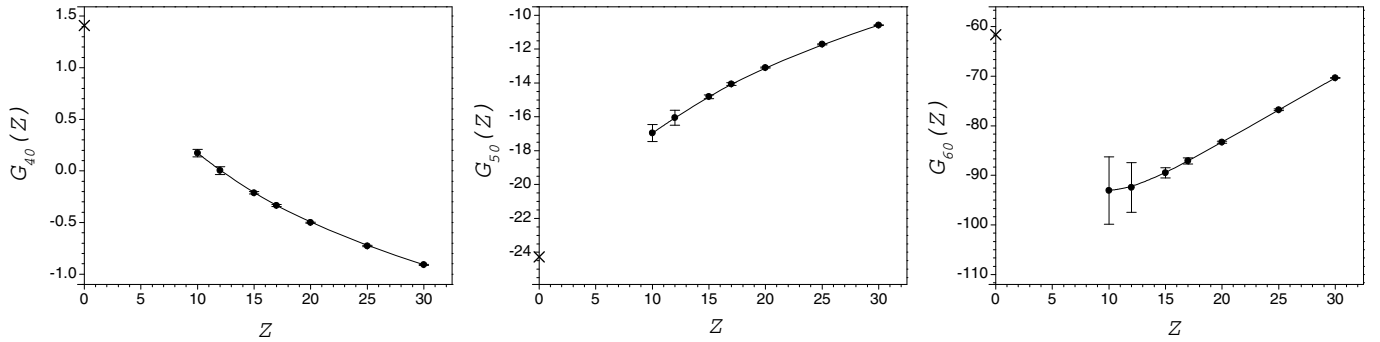


Fig. 3. The two-loop self-energy correction. $G_{40}(Z) = \Delta E/[m\alpha^2(Z\alpha)^4/\pi^2]$, $G_{50}(Z)$ and $G_{60}(Z)$ are defined by equations (44) and (45). The cross on the y -axis indicates the analytical results, $G_{40}(0) = B_{40}$, $G_{50}(0) = B_{50}$, and $G_{60}(0) = B_{60}$.

$$G(E, \mathbf{x}_1, \mathbf{x}_2) = \sum_{\kappa\mu} \begin{pmatrix} G_{\kappa}^{11}(E, \mathbf{x}_1, \mathbf{x}_2) \chi_{\kappa\mu}(\hat{\mathbf{x}}_1) \chi_{\kappa\mu}^{\dagger}(\hat{\mathbf{x}}_2) & G_{\kappa}^{12}(E, \mathbf{x}_1, \mathbf{x}_2) (-i) \chi_{\kappa\mu}(\hat{\mathbf{x}}_1) \chi_{-\kappa\mu}^{\dagger}(\hat{\mathbf{x}}_2) \\ G_{\kappa}^{21}(E, \mathbf{x}_1, \mathbf{x}_2) i \chi_{-\kappa\mu}(\hat{\mathbf{x}}_1) \chi_{\kappa\mu}^{\dagger}(\hat{\mathbf{x}}_2) & G_{\kappa}^{22}(E, \mathbf{x}_1, \mathbf{x}_2) \chi_{-\kappa\mu}(\hat{\mathbf{x}}_1) \chi_{-\kappa\mu}^{\dagger}(\hat{\mathbf{x}}_2) \end{pmatrix} \quad (\text{A.1})$$

two consecutive points from our data set and store the resulting values at $Z = Z_0$. Second, we perform a global parabolic least-squares fit to the set of data obtained on the first step and take the fitted value at $Z = Z_0$ as a final result. Similar procedure applied to the function G_{50} reproduces the analytical result for the coefficient B_{50} with the accuracy of about 1%. For comparison, a global polynomial fit yields a result accurate within 5% only.

When applied to the remainder function $G_{60}(Z)$, the extrapolation procedure described above gives

$$G_{60}(Z = 0) = -84(15), \quad (46)$$

$$G_{60}(Z = 1) = -86(15). \quad (47)$$

The extrapolated value for $Z = 1$ is higher than but marginally consistent with the 2005 result of $-127(42)$ [19]. The shift of the central value is due to two reasons. First, the analytical result for the B_{61} coefficient was recently changed by $\delta B_{61} = -1.4494$ [5], thus pushing the remainder function higher up. Second, the improved numerical accuracy of the present calculation and the increased number of values of Z studied allowed us to identify the upward trend in the numerical data.

The shift of the extrapolated values for G_{60} significantly reduces the disagreement with the analytical calculation [3] reported in reference [19]. The present value of $G_{60}(0) = -84(15)$ is consistent (but still not in perfect agreement) with the analytical result of $B_{60} = -62(9)$.

To complete our analysis of the higher-order two-loop effects in hydrogen, we combine the result for the two-loop self-energy correction obtained in this work (Eq. (47)) with the corresponding contribution induced by the two-loop diagrams with the closed fermion loops reported in reference [22]. So, our estimate of the *total* (non-logarithmic) two-loop contribution to order $m\alpha^2(Z\alpha)^6$ for the ground state of hydrogen is

$$G_{60}(Z = 1, \text{total}) = -86(15) - 15(2) = -101(15). \quad (48)$$

The numerical contribution of this effect is $-10.2(1.5)$ kHz, which is much larger than the error of the experimental determination of the 1S–2S transition frequency in hydrogen [6] (34 Hz) and comparable with the experimental errors for the 2S–12D transitions [34] (7 kHz).

To conclude, in the present investigation, we described in detail the technique of evaluation of Feynman diagrams in the mixed coordinate-momentum representation based on the analytical representation of the bound electron propagators in terms of the Whittaker functions. This technique allowed us to significantly improve the accuracy of the numerical evaluation of the part of the two-loop self-energy correction conventionally termed as the P term. The all-order (in the parameter $Z\alpha$) results are reported for the two-loop self-energy correction for the ground state of hydrogen-like ions with the nuclear charge number $Z = 10$ –30. The higher-order (in $Z\alpha$) remainder function is inferred from the numerical results and extrapolated towards $Z = 0$ and 1. The extrapolated value is in marginal agreement with the analytical result obtained within the perturbative approach.

The work presented in this paper was supported by RFBR (grant No. 10-02-00150-a).

Appendix A: Dirac Coulomb Green function in the coordinate-momentum representation

The Dirac Coulomb Green function is commonly written in coordinate space as an expansion in the relativistic angular momentum parameter κ [11–13,35],

see equation (A.1) above,

where $\chi_{\kappa\mu}(\hat{\mathbf{x}})$ are the Dirac spin-angular spinors [24] and $\hat{\mathbf{x}} = \mathbf{x}/|\mathbf{x}|$. The 2×2 matrix of the radial components G_{κ}^{ij} is referred to as the radial Green function and denoted as

$$G(E, \mathbf{x}_1, \mathbf{p}_2) = \sum_{\kappa\mu} i^l \left(\begin{array}{cc} G_{\kappa}^{11}(E, x_1, p_2) \chi_{\kappa\mu}(\hat{\mathbf{x}}_1) \chi_{\kappa\mu}^{\dagger}(\hat{\mathbf{p}}_2) & G_{\kappa}^{12}(E, x_1, p_2) \chi_{\kappa\mu}(\hat{\mathbf{x}}_1) \chi_{-\kappa\mu}^{\dagger}(\hat{\mathbf{p}}_2) \\ G_{\kappa}^{21}(E, x_1, p_2) i \chi_{-\kappa\mu}(\hat{\mathbf{x}}_1) \chi_{\kappa\mu}^{\dagger}(\hat{\mathbf{p}}_2) & G_{\kappa}^{22}(E, x_1, p_2) i \chi_{-\kappa\mu}(\hat{\mathbf{x}}_1) \chi_{-\kappa\mu}^{\dagger}(\hat{\mathbf{p}}_2) \end{array} \right) \quad (\text{A.6})$$

$$G_{\kappa}(E, x_1, p_2) = 4\pi \int_0^{\infty} dx_2 x_2^2 \left(\begin{array}{cc} j_l(p_2 x_2) G_{\kappa}^{11}(E, x_1, x_2) & -\frac{\kappa}{|\kappa|} j_{\bar{l}}(p_2 x_2) G_{\kappa}^{12}(E, x_1, x_2) \\ j_l(p_2 x_2) G_{\kappa}^{21}(E, x_1, x_2) & -\frac{\kappa}{|\kappa|} j_{\bar{l}}(p_2 x_2) G_{\kappa}^{22}(E, x_1, x_2) \end{array} \right) \quad (\text{A.7})$$

G_{κ} . The radial Green function can be expressed in terms of the two-component solutions of the radial Dirac equation regular at the origin (ϕ_{κ}^0) and the infinity (ϕ_{κ}^{∞}) as follows

$$G_{\kappa}(E, x_1, x_2) = -\phi_{\kappa}^{\infty}(E, x_1) \phi_{\kappa}^{0T}(E, x_2) \theta(x_1 - x_2) - \phi_{\kappa}^0(E, x_1) \phi_{\kappa}^{\infty T}(E, x_2) \theta(x_2 - x_1). \quad (\text{A.2})$$

The upper and the lower components of the functions ϕ_{κ}^0 and ϕ_{κ}^{∞} will be denoted by subscripts “+” and “−”, respectively. They are given by

$$\phi_{\kappa, \pm}^0(E, x) = \Delta_{\kappa}^{-1/2} \frac{\sqrt{1 \pm E}}{x^{3/2}} \left[(\lambda - \nu) M_{\nu - \frac{1}{2}, \lambda}(2cx) \mp \left(\kappa - \frac{\alpha Z}{c} \right) M_{\nu + \frac{1}{2}, \lambda}(2cx) \right], \quad (\text{A.3})$$

$$\phi_{\kappa, \pm}^{\infty}(E, x) = \Delta_{\kappa}^{-1/2} \frac{\sqrt{1 \pm E}}{x^{3/2}} \left[\left(\kappa + \frac{\alpha Z}{c} \right) W_{\nu - \frac{1}{2}, \lambda}(2cx) \pm W_{\nu + \frac{1}{2}, \lambda}(2cx) \right], \quad (\text{A.4})$$

where $\Delta_{\kappa} = 4c^2 \Gamma(1 + 2\lambda) / \Gamma(\lambda - \nu)$, $c = \sqrt{1 - E^2}$ defined so that $\text{Re}(c) > 0$, $\lambda = \sqrt{\kappa^2 - (Z\alpha)^2}$, $\nu = Z\alpha E / c$, and $M_{\alpha, \beta}$ and $W_{\alpha, \beta}$ are the Whittaker functions of the first and the second kind, respectively.

The Dirac Coulomb Green function in the coordinate-momentum representation is obtained from the above formulas by the Fourier transform over one of the radial arguments. Let us consider the transform over, e.g., the second radial argument,

$$G(E, \mathbf{x}_1, \mathbf{p}_2) = \int d\mathbf{x}_2 e^{i\mathbf{p}_2 \cdot \mathbf{x}_2} G(E, \mathbf{x}_1, \mathbf{x}_2). \quad (\text{A.5})$$

Its partial-wave expansion takes the form

see equation (A.6) above,

with the radial part given by the following matrix

see equation (A.7) above,

where $l = |\kappa + 1/2| - 1/2$ and $\bar{l} = |\kappa - 1/2| - 1/2$. Using equation (A.2), we obtain the following representation for the radial Green function in the mixed coordinate-momentum representation,

$$G_{\kappa}(E, x_1, p_2) = -\phi_{\kappa}^{\infty}(E, x_1) \psi_{\kappa}^{0T}(E, p_2; x_1) - \phi_{\kappa}^0(E, x_1) \psi_{\kappa}^{\infty T}(E, p_2; x_1), \quad (\text{A.8})$$

where

$$\psi_{\kappa}^0(E, p; x_1) = 4\pi \int_0^{x_1} dx_2 x_2^2 \left(\begin{array}{c} j_l(p x_2) \phi_{\kappa, +}^0(E, x_2) \\ -\frac{\kappa}{|\kappa|} j_{\bar{l}}(p x_2) \phi_{\kappa, -}^0(E, x_2) \end{array} \right), \quad (\text{A.9})$$

and

$$\psi_{\kappa}^{\infty}(E, p; x_1) = 4\pi \int_{x_1}^{\infty} dx_2 x_2^2 \left(\begin{array}{c} j_l(p x_2) \phi_{\kappa, +}^{\infty}(E, x_2) \\ -\frac{\kappa}{|\kappa|} j_{\bar{l}}(p x_2) \phi_{\kappa, -}^{\infty}(E, x_2) \end{array} \right). \quad (\text{A.10})$$

The integration over x_2 in the functions ψ_{κ}^0 and ψ_{κ}^{∞} has to be performed numerically. The problems here are that (i) the integration interval depends on x_1 and (ii) the integrand contains the spherical Bessel function which oscillates rapidly in the high-momenta region. Clearly, a straightforward use of equations (A.9) and (A.10) in our calculations would lead to a re-evaluation of the integral for each new value of x_1 , making the computation prohibitively expensive. One can observe, however, that if the function $\psi_{\kappa}(E, p; x)$ is known for a particular set of E , p , and x , then the evaluation of $\psi_{\kappa}(E, p; x')$ can be done by computing the Bessel transform integral over the interval (x, x') only. So, introducing an ordered radial grid $\{x_i\}$, one can store the whole set of values $\{\psi_{\kappa}(E, p; x_i)\}$ by performing just one Bessel transform over the interval $(0, \infty)$. This shows that for a fixed values of E and p , the integrations of the type $\int_0^{\infty} dx f(x) \psi_{\kappa}(E, p; x)$ can be performed without a recalculation of the Bessel transform integral.

Appendix B: Free Dirac Green function in the coordinate-momentum representation

The free Dirac Green function $G^{(0)}$ is a much simpler object than the Dirac Coulomb Green function G and is known in the closed analytical form as well as in the partial-wave expansion form (see, e.g., Ref. [12,13]). For the purposes of the present investigation, we employ the coordinate-momentum representation and put $G^{(0)}$ into the form analogous to equations (A.6) and (A.7). The simplest way to achieve this is to start with the momentum representation of $G^{(0)}$, which has a particularly simple form,

$$G^{(0)}(E, \mathbf{p}_1, \mathbf{p}_2) = (2\pi)^3 \frac{\delta^3(\mathbf{p}_1 - \mathbf{p}_2)}{\gamma^0 E - \boldsymbol{\gamma} \cdot \mathbf{p}_2 - m} \gamma^0 = (2\pi)^3 \frac{E + \boldsymbol{\alpha} \cdot \mathbf{p}_2 + m \gamma^0}{E^2 - \mathbf{p}_2^2 - m^2} \delta^3(\mathbf{p}_1 - \mathbf{p}_2), \quad (\text{B.1})$$

$$G^{(0)}(E, \mathbf{p}_1, \mathbf{p}_2) = (2\pi)^3 \frac{\frac{1}{p_2^2} \delta(p_1 - p_2)}{E^2 - p_2^2 - m^2} \sum_{\kappa\mu} \begin{pmatrix} (E+m) \chi_{\kappa\mu}(\hat{\mathbf{p}}_1) \chi_{\kappa\mu}^\dagger(\hat{\mathbf{p}}_2) & -p_2 \chi_{\kappa\mu}(\hat{\mathbf{p}}_1) \chi_{-\kappa\mu}^\dagger(\hat{\mathbf{p}}_2) \\ -p_2 \chi_{-\kappa\mu}(\hat{\mathbf{p}}_1) \chi_{\kappa\mu}^\dagger(\hat{\mathbf{p}}_2) & (E-m) \chi_{-\kappa\mu}(\hat{\mathbf{p}}_1) \chi_{-\kappa\mu}^\dagger(\hat{\mathbf{p}}_2) \end{pmatrix} \quad (\text{B.3})$$

$$G_\kappa^{(0)}(E, x_1, p_2) = \frac{4\pi}{E^2 - p_2^2 - m^2} \begin{pmatrix} (E+m) j_l(p_2 x_1) & -p_2 j_l(p_2 x_1) \\ \frac{\kappa}{|\kappa|} p_2 j_{\bar{l}}(p_2 x_1) & -\frac{\kappa}{|\kappa|} (E-m) j_{\bar{l}}(p_2 x_1) \end{pmatrix} \quad (\text{B.5})$$

where $\boldsymbol{\alpha} = \gamma^0 \boldsymbol{\gamma}$. Using the completeness of the angular-momentum spinors $\chi_{\kappa\mu}$,

$$\sum_{\kappa\mu} \chi_{\kappa\mu}(\hat{\mathbf{p}}_1) \chi_{\kappa\mu}^\dagger(\hat{\mathbf{p}}_2) = I \delta(\hat{\mathbf{p}}_1 - \hat{\mathbf{p}}_2), \quad (\text{B.2})$$

and the identity $(\boldsymbol{\sigma} \cdot \hat{\mathbf{p}}) \chi_{\kappa\mu}(\hat{\mathbf{p}}) = -\chi_{-\kappa\mu}(\hat{\mathbf{p}})$, we cast equation (B.1) into the partial-wave expansion form similar to that for the Dirac Coulomb Green function,

see equation (B.3) above,

where $p_i = |\mathbf{p}_i|$. The coordinate-momentum representation of $G^{(0)}$ is obtained by the Fourier transform of the above expression over the first radial argument,

$$G^{(0)}(E, \mathbf{x}_1, \mathbf{p}_2) = \int \frac{d\mathbf{p}_1}{(2\pi)^3} e^{i\mathbf{p}_1 \cdot \mathbf{x}_1} G^{(0)}(E, \mathbf{p}_1, \mathbf{p}_2). \quad (\text{B.4})$$

After performing the integration over \mathbf{p}_1 , the free Dirac Green function is written in the form of equation (A.6), with the radial part given by

see equation (B.5) above.

Appendix C: Angular factors

In this section we address the factors t_{κ_n, κ_a} and s_{κ_n, κ_a}^k , which are defined by equations (35)–(37). Inserting the explicit definitions of the angular-momentum spinors in these formulas, averaging over the angular momentum projections of the reference state, and calculating the sums of the Clebsch-Gordan coefficients, we arrive at the following results,

$$t_{\kappa_n, \kappa_a}(J) = \frac{(-1)^{j_a+1/2}}{\sqrt{4\pi}} \frac{\Pi_{j_n}}{\Pi_{j_a}} \begin{Bmatrix} j_a & j_n & J \\ l_n & l_a & 1/2 \end{Bmatrix} \times \sum_M (-1)^M Y_{JM}(\hat{\mathbf{q}}) Y_{l_n l_a}^{J-M}(\hat{\mathbf{p}}_1, \hat{\mathbf{p}}_2), \quad (\text{C.1})$$

$$s_{\kappa_n, \kappa_a}^\sigma(JL) = (-1)^{l_n+L} \sqrt{\frac{6}{4\pi}} \frac{\Pi_{j_n J J}}{\Pi_{j_a L}} \begin{Bmatrix} j_a & j_n & J \\ 1/2 & 1/2 & 1 \\ l_a & l_n & L \end{Bmatrix} \times \sum_M (-1)^M Y_{LM}(\hat{\mathbf{q}}) Y_{l_n l_a}^{L-M}(\hat{\mathbf{p}}_1, \hat{\mathbf{p}}_2), \quad (\text{C.2})$$

$$s_{\kappa_n, \kappa_a}^{p_1}(JL) = \frac{(-1)^{j_a+1/2}}{\sqrt{3}} \frac{\Pi_{j_n}}{\Pi_{j_a}} \begin{Bmatrix} j_a & j_n & J \\ l_n & l_a & 1/2 \end{Bmatrix} \times \sum_M (-1)^M Y_{L1}^{JM}(\hat{\mathbf{q}}, \hat{\mathbf{p}}_1) Y_{l_n l_a}^{J-M}(\hat{\mathbf{p}}_1, \hat{\mathbf{p}}_2), \quad (\text{C.3})$$

$$s_{\kappa_n, \kappa_a}^{p_2}(JL) = \frac{(-1)^{j_a+1/2}}{\sqrt{3}} \frac{\Pi_{j_n}}{\Pi_{j_a}} \begin{Bmatrix} j_a & j_n & J \\ l_n & l_a & 1/2 \end{Bmatrix} \times \sum_M (-1)^M Y_{L1}^{JM}(\hat{\mathbf{q}}, \hat{\mathbf{p}}_2) Y_{l_n l_a}^{J-M}(\hat{\mathbf{p}}_1, \hat{\mathbf{p}}_2), \quad (\text{C.4})$$

where $\Pi_{j_1, j_2, \dots} = \sqrt{(2j_1+1)(2j_2+1)\dots}$ and $Y_{l_1 l_2}^{JM}(\hat{\mathbf{p}}_1, \hat{\mathbf{p}}_2)$ are the bipolar spherical harmonics [26].

With help of formulas from the book [26], it is possible to obtain explicit results for the angular factors t_{κ_n, κ_a} and s_{κ_n, κ_a}^k , which are functions of $p_1 = |\mathbf{p}_1|$, $p_2 = |\mathbf{p}_2|$, and $q = |\mathbf{p}_1 - \mathbf{p}_2|$ only. However, the resulting formulas turn out to be rather lengthy and not very convenient for numerical evaluation as they become numerically unstable for $q \rightarrow 0$. Because of this, we prefer to evaluate equations (C.1)–(C.4) numerically, after some simplifications that exploit the fact that the result does not depend on any angles except for $\hat{\mathbf{p}}_1 \cdot \hat{\mathbf{p}}_2$. Namely, we set the azimuthal spherical coordinate of $\hat{\mathbf{p}}_1$ and $\hat{\mathbf{p}}_2$ to zero ($\phi_1 = \phi_2 = 0$) and direct $\hat{\mathbf{p}}_1$ along the z axis (setting $\theta_1 = 0$).

References

1. P.J. Mohr, B.N. Taylor, D.B. Newell, Rev. Mod. Phys. **80**, 633 (2008)
2. K. Pachucki, Phys. Rev. A **63**, 042503 (2001)
3. K. Pachucki, U.D. Jentschura, Phys. Rev. Lett. **91**, 113005 (2003)
4. A. Czarnecki, U.D. Jentschura, K. Pachucki, Phys. Rev. Lett. **95**, 180404 (2005)
5. U.D. Jentschura, A. Czarnecki, K. Pachucki, Phys. Rev. A **72**, 062102 (2005)
6. M. Fischer et al., Phys. Rev. Lett. **92**, 230802 (2004)
7. I. Draganić, J.R. Crespo López-Urrutia, R. DuBois, S. Fritzsche, V.M. Shabaev, R.S. Orts, I.I. Tupitsyn, Y. Zou, J. Ullrich, Phys. Rev. Lett. **91**, 183001 (2003)
8. C. Brandau et al., Phys. Rev. Lett. **91**, 073202 (2003)
9. P. Beiersdorfer, H. Chen, D.B. Thorn, E. Träbert, Phys. Rev. Lett. **95**, 233003 (2005)
10. S.W. Epp et al., Phys. Rev. Lett. **98**, 183001 (2007)
11. E.H. Wichmann, N.M. Kroll, Phys. Rev. A **101**, 843 (1956)
12. P.J. Mohr, Ann. Phys. (NY) **88**, 26 (1974)
13. P.J. Mohr, Ann. Phys. (NY) **88**, 52 (1974)
14. A.M. Desiderio, W.R. Johnson, Phys. Rev. A **3**, 1267 (1971)
15. S. Mallampalli, J. Sapirstein, Phys. Rev. A **57**, 1548 (1998)
16. V.A. Yerokhin, V.M. Shabaev, Phys. Rev. A **64**, 062507 (2001)

17. V.A. Yerokhin, P. Indelicato, V.M. Shabaev, Phys. Rev. Lett. **91**, 073001 (2003)
18. V.A. Yerokhin, P. Indelicato, V.M. Shabaev, Eur. Phys. J. D **25**, 203 (2003)
19. V.A. Yerokhin, P. Indelicato, V.M. Shabaev, Phys. Rev. A **71**, R040101 (2005)
20. V.A. Yerokhin, P. Indelicato, V.M. Shabaev, Phys. Rev. Lett. **97**, 253004 (2006)
21. V.A. Yerokhin, Phys. Rev. A **80**, 040501(R) (2009)
22. V.A. Yerokhin, P. Indelicato, V.M. Shabaev, Phys. Rev. A **77**, 062510 (2008)
23. V.A. Yerokhin, V.M. Shabaev, Phys. Rev. A **60**, 800 (1999)
24. M.E. Rose, *Relativistic Electron Theory* (John Wiley & Sons, New York, 1961)
25. W.R. Johnson, S.A. Blundell, J. Sapirstein, Phys. Rev. A **37**, 2764 (1988)
26. D.A. Varshalovich, A.N. Moskalev, V.K. Khersonskii, *Quantum Theory of Angular Momentum* (World Scientific, Singapore, 1988)
27. V.A. Yerokhin, A.N. Artemyev, T. Beier, G. Plunien, V.M. Shabaev, G. Soff, Phys. Rev. A **60**, 3522 (1999)
28. T. Appelquist, S.J. Brodsky, Phys. Rev. A **2**, 2293 (1970)
29. K. Pachucki, Phys. Rev. Lett. **72**, 3154 (1994)
30. M.I. Eides, V.A. Shelyuto, Phys. Rev. A **52**, 954 (1995)
31. S.G. Karshenbojm, Zh. Eksp. Teor. Fiz. **103**, 1105 (1993) [JETP **76**, 541 (1993)]
32. V.A. Yerokhin, Phys. Rev. Lett. **86**, 1990 (2001)
33. P.J. Mohr, Phys. Rev. Lett. **34**, 1050 (1975)
34. C. Schwob, L. Jozefowski, B. de Beauvoir, L. Hilico, F. Nez, L. Julien, F. Biraben, O. Acaf, J.J. Zondy, A. Clairon, Phys. Rev. Lett. **82**, 4960 (1999)
35. P.J. Mohr, G. Plunien, G. Soff, Phys. Rep. **293**, 227 (1998)